chemistry proceedings

MDPI

Proceeding Paper

Fabrication and Characterization of Lanthanoid-Doped Perovskite Solar Cells †

Ryushi Nakamura [1], Atsushi Suzuki [1,*], Takeo Oku [1], Tomoharu Tachikawa [2] and Sakiko Fukunishi [2]

[1] Department of Materials Chemistry, The University of Shiga Prefecture, Hikone 522-8533, Japan; tt21rnakamura@ec.usp.ac.jp (R.N.); oku@mat.usp.ac.jp (T.O.)
[2] Osaka Gas Chemicals Co., Ltd., Osaka 554-0051, Japan
* Correspondence: suzuki@mat.usp.ac.jp
† Presented at the 5th International Online Conference on Crystals, 15–17 June 2026; Available online: https://sciforum.net/event/IOCC2026.

Abstract

Perovskite solar cells (PSCs) are promising photovoltaic devices, but their practical application is limited by structural instability and ion migration. This study investigates the effects of Gd incorporation on $MA_{0.75}FA_{0.25}PbI_3$ using optical characterization and first-principles calculations. Optical microscopy revealed changes in film morphology, while UV–vis spectroscopy showed enhanced near-infrared absorption without a significant change in the optical bandgap. Density functional theory indicated bandgap narrowing due to Gd-induced lattice distortion. Furthermore, Born–Oppenheimer molecular dynamics and Car–Parrinello molecular dynamics simulations revealed increased atomic diffusion, higher enthalpy, and enhanced lattice fluctuations. These results demonstrate that Gd modifies the electronic structure and lattice dynamics of perovskite materials.

Keywords: perovskite solar cell; lanthanoid; molecular dynamics calculation; gadolinium

1. Introduction

Perovskite solar cells are attracting attention as next-generation solar cells due to their flexibility and light weight [1–5]. However, challenges remain, such as long-term degradation caused by ion migration and a decrease in the fill factor and open-circuit voltage due to defects [6–10]. Additive engineering is particularly attractive because the incorporation of a small amount of functional species can modify the crystallization process, regulate defect formation, and influence the chemical environment within the perovskite lattice without substantially changing the overall device architecture [11]. Previous research has investigated the substitution of A- and B-sites with alkali metal and transition metal elements as effective strategies [12–16]. In particular, lanthanide elements have the potential to influence lattice strain, electronic states, and ion migration [6,17–20]. Since Gd has a different ionic radius than Pb, it is highly likely to alter lattice strain, local structure, and dynamic behavior [21–24]. Such interactions can alter the local coordination environment of the perovskite lattice, potentially reducing under-coordinated sites and suppressing pathways associated with ion migration and non-radiative recombination. However, while many studies have reported changes in optical properties and device performance, the effects on lattice dynamics, ion diffusion, and optical response have not been thoroughly investigated [25–28].

In our previous study, we investigated the effects of Gd doping on surface morphology, microstructure, and photovoltaic characteristics using Scanning Electric Microscopy, X-Ray

Academic Editor: Zongyou Yin

Published: 16 September 2026

Diffraction (XRD), Current Density-Voltage, and External Quantum Efficiency measurements. However, we did not conduct an in-depth investigation of the effects on lattice dynamics, ion diffusion, and optical response [20,29–32]. First-principles calculations provide a complementary approach for understanding how dopant incorporation modifies the electronic structure and local atomic environment of perovskite materials. Such theoretical analysis can provide microscopic insight into experimentally observed changes in optical and photovoltaic properties, which cannot always be directly determined from macroscopic measurements [33].

In this study, we aim to analyze Gd-doped perovskites by combining optical microscopy, absorbance measurements, dielectric function calculations, and Born–Oppenheimer molecular dynamics (BOMD) and Car–Parrinello molecular dynamics (CPMD). We elucidate how Gd-induced lattice strain affects the band structure, ion mobility, and thermodynamic stability, thereby providing an atomistic understanding of dopant-induced perturbations in perovskites.

2. Calculation and Experimental Methods

The surface morphology of the perovskite layer was examined using bright-field transmission and reflection microscopy with an optical microscope (Nikon, Tokyo, Japan, Eclipse E600) and a universal reflected illumination unit (Nikon, LV-UEPI, 50 W). The device structure used for the measurements was FTO/TiO_2/Perovskite/Decphenyicycyclopentasilane (Osaka Gas Chemicals, Osaka, Japan, OGSOL SI-30-15)/Spiro-OMeTAD (Sigma-Aldrich, Tokyo, Japan). $(CH_3NH_3)_{0.75}[CH(NH_2)_2]_{0.25}PbI_3$ perovskite precursor solution was prepared by mixing CH_3NH_3I (Tokyo Chemical Industry, Tokyo, Japan, 174.9 mg), $CH(NH_2)_2I$ (Sigma-Aldrich, Tokyo, Japan, 17.2 mg), and $PbCl_2$ (Sigma-Aldrich, Tokyo, Japan 111.24 mg) in N,N-dimethylformamide (Sigma-Aldrich) at 60 °C for approximately 24 h. Lanthanide compounds, including 1% $CeCl_3$ (Tokyo Kasei Kogyo Co., Ltd., Tokyo, Japan), $ErCl_3$ (Tokyo Kasei Kogyo Co., Ltd., Tokyo, Japan), NdF_3 (Sigma-Aldrich, Tokyo, Japan), $YbCl_3$ (Tokyo Kasei Kogyo Co., Ltd., Tokyo, Japan), and GdF_3 (Tokyo Chemical Industry, Tokyo, Japan), were added to the Pb sites, which reduced the $PbCl_2$ concentration by 1%.

The perovskite precursor solution was spin-coated three times at 2000 rpm for 60 s onto a mesoporous TiO_2 layer at 90 °C employing the air-blow method. The resulting film thickness was approximately 500 nm. A decaphenylcyclopentasilane solution, prepared by stirring decaphenylcyclopentasilane (10 mg) in chlorobenzene (Wako Pure Chemical Industries, Osaka, Japan, 0.5 mL), was spin-coated at 2000 rpm for 60 s. The cells were subsequently heat-treated at 190 °C.

The optical properties of the perovskite layer were measured using a UV-Vis spectrophotometer (JASCO, Tokyo, Japan, V-700). The transmittance T across the measurement wavelength range was obtained, and absorption A was calculated using the following equation.

$$A = -\log_{10} T \quad (1)$$

Here, T represents the transmittance. We plotted the Tauc curve based on the obtained absorption spectrum and evaluated the optical bandgap.

First-principles calculations were performed based on Density Functional Theory (DFT). A $2 \times 2 \times 2$ supercell was constructed based on the lattice constants and crystal structure obtained from XRD. In this study, to evaluate the electronic states that reflect the experimental structure, no structural optimization was performed; instead, electronic structure calculations were carried out using the constructed supercell.

The same supercell was used for dielectric function calculations, BOMD, and CPMD simulations. The Perdew–Burke–Ernzerhof (PBE) exchange-correlation functional was adopted, and the pbe-mt_fhi.UPF pseudopotential was used. The kinetic energy cutoff for

the plane-wave basis set was set to 50 Ry for $MAPbI_3$ and 35 Ry for $MAPb_{0.875}Gd_{0.125}I_3$, while the charge density cutoff was set to 450 Ry and 315 Ry, respectively. These values were determined based on convergence calculations for each model. A 2 × 2 × 2 k-point grid based on the Monkhorst–Pack method was used for Brillouin zone sampling. No smearing was applied to the occupation numbers, and the number of bands was set to 30% higher than the required number for each calculation. BOMD calculations were performed at 300 K with a time step of 0.2419 fs and a calculation time of 200 steps (0.0486 ps). The diffusion coefficients for each atom were calculated using Einstein's equation based on the time evolution of the mean square displacement. Since this study employed a pseudopotential that treats the 4f electrons of Gd as itinerant electrons, the DFT+U method was not applied. Furthermore, no spin-polarized calculations were performed, and the electronic structure was evaluated in the non-magnetic state.

3. Results and Discussion

Figure 1 shows optical microscopy images of the perovskite films under bright-field transmission and reflection modes. The Gd-containing film exhibited a darker optical contrast than the standard film, indicating a noticeable change in the appearance of the perovskite layer after Gd incorporation. In contrast, the Yb-added sample shows yellowish regions, which may be associated with residual PbI_2. The presence of PbI_2 in the corresponding perovskite films was confirmed by XRD in our previous study [29]. However, this assignment is tentative because it is based on optical microscopy alone. Furthermore, localized dark spots were observed in the Er- and Yb-containing films, which may be associated with spatial variations in grain formation and film morphology. Although these observations suggest dopant-dependent microstructural variation, a definitive phase assignment is beyond the scope of this work and is discussed in Ref. [29].

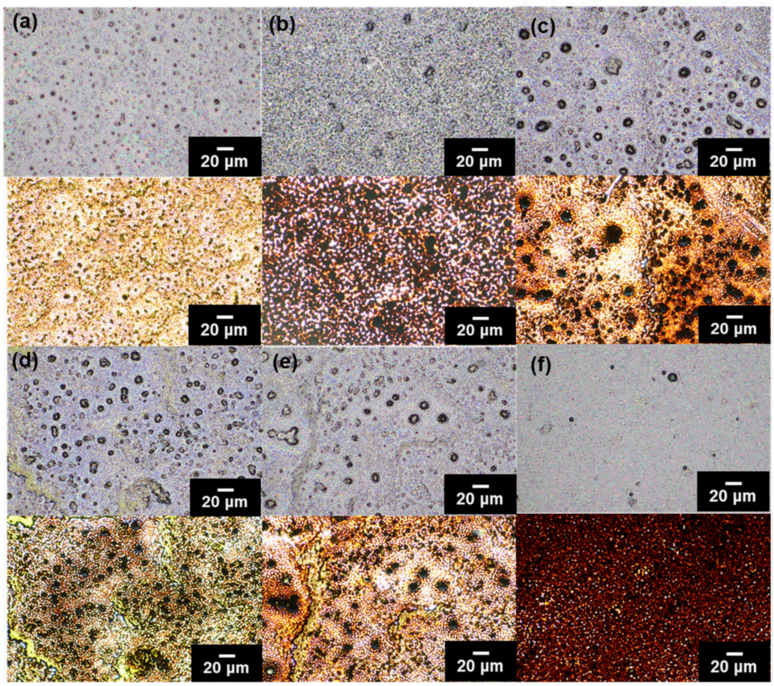

Figure 1. Optical microscope images of perovskite solar cells. (**a**) Standard, (**b**) +Ce, (**c**) +Er, (**d**) +Yb, (**e**) +Nd, and (**f**) +Gd perovskite.

To investigate the effect of Gd incorporation on optical properties, UV–vis absorption spectra, transmittance spectra, and Tauc plots were analyzed (Figure 2a,b). No significant change in the optical bandgap was observed between the standard and Gd doped sam-

ples, indicating that the fundamental absorption edge is largely preserved upon doping. However, an enhanced absorption in the near-infrared region was observed for the Gd-containing system. This trend suggests that Gd incorporation modifies the optical response, possibly through changes in light scattering, sub-gap absorption states, or film thickness effects reported in Ref. [29].

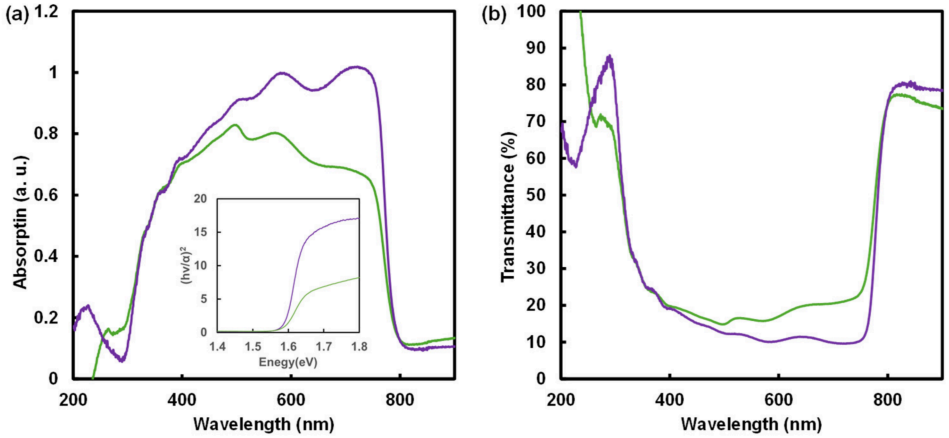

Figure 2. (**a**) UV-vis absorption spectra with Tauc-plot and (**b**) transmittance of the perovskite solar cells. Purple line: Gd doping, green line: standard.

To clarify the origin of the optical response, DFT calculations were performed for $MA_{0.75}FA_{0.25}PbI_3$ and $MA_{0.75}FA_{0.25}Pb_{0.875}Gd_{0.125}I_3$. The calculated Tauc plots (Figure 3) indicate bandgap values of 2.14 eV and 1.90 eV, respectively, suggesting a reduction in the bandgap upon Gd substitution. This trend is attributed to local structural distortion induced by Gd incorporation, which modifies the electronic states near the band edges. Rather than a direct contribution of Gd 4f orbitals, the bandgap modulation is more likely governed by changes in Pb–I bonding geometry and associated electronic redistribution. The difference between the experimentally determined optical bandgap and the DFT-calculated bandgap can be attributed to several factors. First, the Gd concentration used in the theoretical model was higher than that used experimentally because modeling the experimentally relevant low dopant concentration would require a substantially larger supercell and consequently a much higher computational cost. Therefore, the calculated bandgap should not be regarded as a direct quantitative representation of the experimental value. Second, the PBE functional employed in the present DFT calculations has inherent limitations in describing semiconductor bandgaps. Furthermore, the theoretical model represents an idealized crystalline structure, whereas the experimentally prepared perovskite films contain defects, local structural distortions, grain boundaries, and thermal fluctuations. These differences in composition and structural environment can contribute to the discrepancy between the calculated and experimental bandgap values. Nevertheless, the theoretical results provide useful insight into the changes in electronic structure induced by Gd incorporation.

BOMD simulations were performed at 300 K to investigate atomic motion in the time range of 0–0.05 ps (Figure 4). The atomic trajectories indicate thermally activated fluctuations within both organic and inorganic sublattices. The calculated diffusion coefficients (Table 1) show that H, C, I, and N species exhibit increased mobility upon Gd incorporation. This suggests that Gd doping modifies the local lattice dynamics, potentially influencing ionic transport pathways and defect-mediated diffusion processes. Such an enhancement in diffusion behavior may reflect either increased ionic mobility or reduced lattice rigidity, depending on the balance between structural stabilization and dynamic disorder.

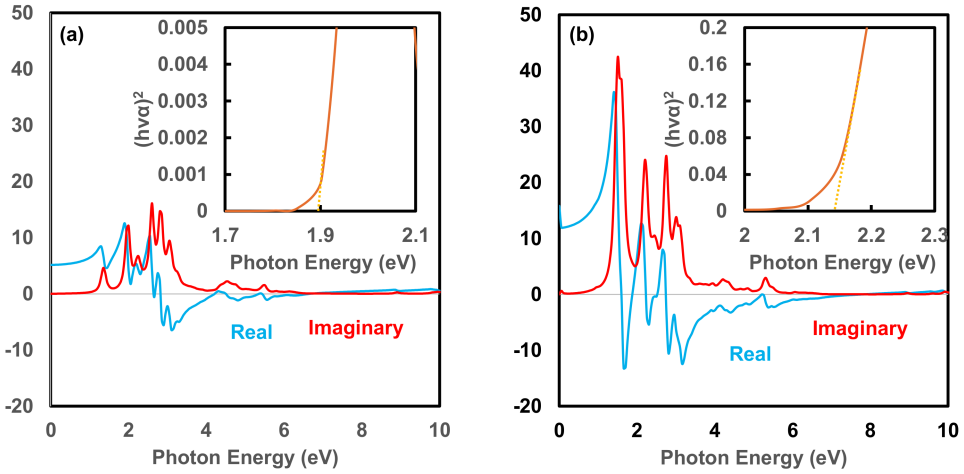

Figure 3. Dielectric function (inserted figure: Tauc-plot) of (**a**) $MA_{0.75}FA_{0.25}PbI_3$ and (**b**) $MA_{0.75}FA_{0.25}Pb_{0.875}Gd_{0.125}I_3$.

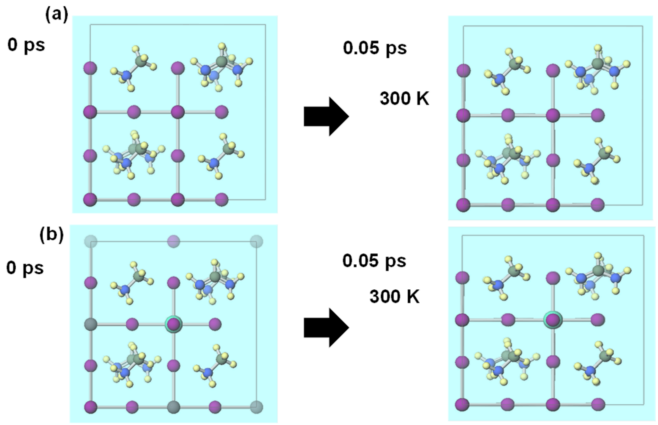

Figure 4. Changes in atomic arrangement obtained by BOMD calculations: (**a**) $MA_{0.75}FA_{0.25}PbI_3$ and (**b**) $MA_{0.75}FA_{0.25}Pb_{0.875}Gd_{0.125}I_3$.

Table 1. Diffusion coefficients obtained by BOMD calculations.

Crystal Model	E_{tot} (eV Cell^{-1})	D ($\times 10^{-6}$ cm^2 s^{-1})				
		H	Pb	C	I	N
$MA_{0.75}FA_{0.25}PbI_3$	−3569	6.83	0.02	0.40	0.06	2.82
$MA_{0.75}FA_{0.25}Pb_{0.875}Gd_{0.125}I_3$	−3795	8.53	0.02	0.76	0.37	4.76

Figure 5 compares the time evolution of enthalpy obtained from CPMD simulations for the standard and Gd-substituted systems. The Gd-containing system exhibits a higher average enthalpy, indicating an energetically less stable but more dynamically activated configuration. This behavior suggests that Gd incorporation induces additional lattice perturbations, possibly increasing local strain and configurational disorder. Furthermore, Figure 6 presents the temporal evolution of bond lengths and bond angles for Pb–I and Gd–I coordination environments. The results indicate enhanced positional fluctuations in the Gd-containing system, particularly along Cartesian coordinates, while angular variations remain relatively comparable. These results collectively suggest that Gd incorporation primarily affects translational lattice dynamics rather than angular structural stability.

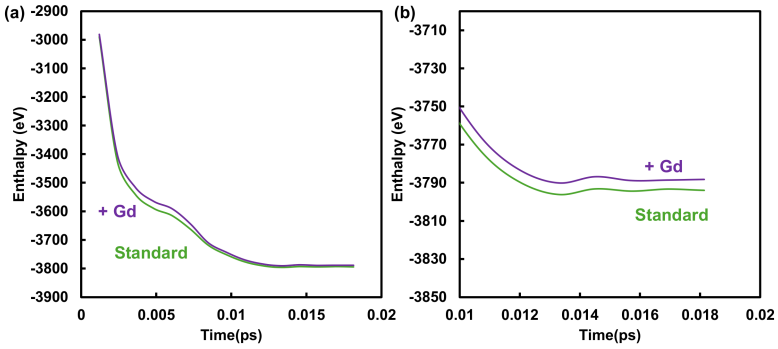

Figure 5. Changes in enthalpy over time by CPMD calculations for crystals. (**a**) relaxation process and (**b**) enlarged view.

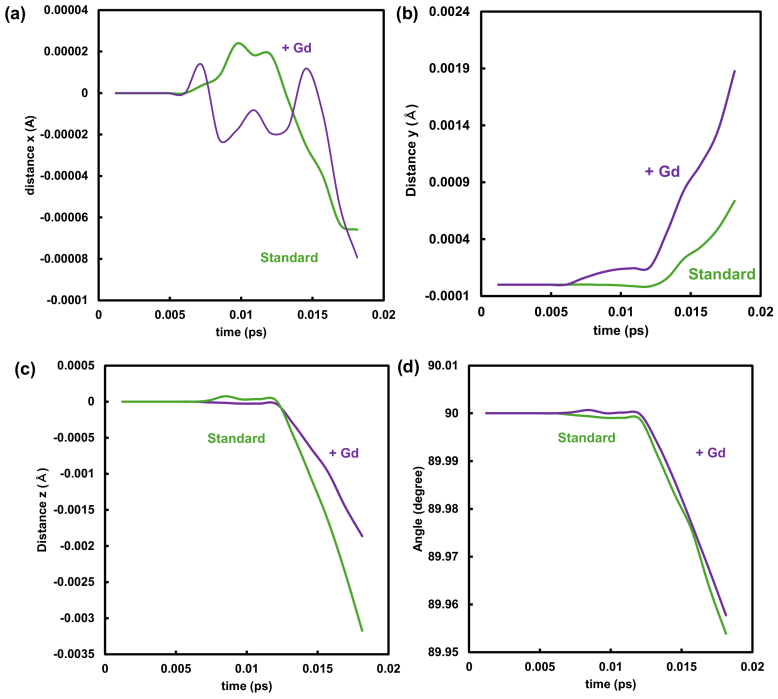

Figure 6. Changes in I-Pb and I-Gd distances of (**a**) x axis, (**b**) y axis and (**c**) z axis (**d**) angles of I-Pb-I and I-Gd-I over time by CPMD calculations for crystals.

4. Conclusions

In this study, we investigated the effects of Gd incorporation on the structural, optical, and atomic-scale properties of $MA_{0.75}FA_{0.25}PbI_3$ perovskite through optical characterization and first-principles calculations. Optical microscopy revealed that Gd incorporation influenced the film morphology, while UV–vis spectroscopy showed that the optical bandgap remained nearly unchanged despite an enhancement in near-infrared absorption. First-principles calculations suggested that Gd substitution alters the local electronic structure through lattice strain, resulting in a decrease in the calculated bandgap. Furthermore, BOMD simulations showed that Gd incorporation increases the diffusion coefficients of H, C, I, and N atoms. CPMD simulations revealed an increase in enthalpy and lattice fluctuations. These results indicate that Gd acts not only as a dopant but also as a modifier of lattice dynamics and electronic structure. By combining experimental and theoretical analyses, we have gained new insights into the relationship between atomic-scale structural dynamics and the optical properties of Gd-doped perovskite materials. In future research, we plan to clarify the correlation between these atomic properties and solar power generation performance, and focus on optimizing rare-earth-doped perovskite solar cells.

https://doi.org/10.3390/chemproc2026021006

Author Contributions: R.N.: Methodology, Software, Formal analysis, Investigation, Writing—original draft preparation. A.S.: Conceptualization, Methodology, Software, Formal analysis, Writing—original draft preparation, Writing—review and editing. T.O.: Conceptualization, Methodology, Writing—original draft preparation, Writing—review and editing, Supervision. T.T.: Resources, Writing—review and editing. S.F.: Resources, Writing—review and editing. All authors have read and agreed to the published version of the manuscript.

Funding: This research received no external funding.

Institutional Review Board Statement: Not applicable.

Informed Consent Statement: Not applicable.

Data Availability Statement: The original contributions presented in this study are included in the article. Further inquiries can be directed to the corresponding author.

Conflicts of Interest: Tomoharu Tachikawa and Sakiko Fukunishi are employed by Osaka Gas Chemicals Co., Ltd. The remaining authors declare that the research was conducted in the absence of any commercial or financial relationships that could be construed as a potential conflict of interest.

References

1. Mishra, A.; Ahmad, Z.; Touati, F.; Shakoor, R.A.; Nazeeruddin, M.K. One-dimensional facile growth of $MAPbI_3$ perovskite micro-rods. *RSC Adv.* **2019**, *9*, 11589–11594. [CrossRef] [PubMed]
2. Zheng, H.; Liu, Y.; Sun, J. Micron-sized columnar grains of $CH_3NH_3PbI_3$ grown by solvent-vapor assisted low-temperature (75 °C) solid-state reaction: The role of non-coordinating solvent-vapor. *Appl. Surf. Sci.* **2018**, *437*, 82–91. [CrossRef]
3. Kırbıyık Kurukavak, Ç.; Yılmaz, T.; Büyükbekar, A.; Tok, M.; Kuş, M. Phosphorus doped carbon dots additive improves the performance of perovskite solar cells via defect passivation in $MAPbI_3$ films. *Mater. Today Commun.* **2023**, *35*, 105668. [CrossRef]
4. Liu, H.; Xiang, L.; Liu, Q.; Gao, P.; Zhang, Y.; Li, S.; Gao, F. Toward high-performance HTL-free all-perovskite tandem solar cells: SCAPS simulation. *IEEE J. Photovolt.* **2024**, *14*, 59–64. [CrossRef]
5. Keeble, D.J.; Wiktor, J.; Pathak, S.K.; Phillips, L.J.; Dickmann, M.; Durose, K.; Snaith, H.J.; Egger, W. Identification of lead vacancy defects in lead halide perovskites. *Nat. Commun.* **2021**, *12*, 5566. [CrossRef] [PubMed]
6. Hussain, T.; Fatima, K.; Anjum, A.; Ali Abbas, T.; Ahmad, I.; Fakharuddin, A.; Sultan, M. Experimental evidence of ion migration in aged inorganic perovskite solar cells using non-destructive RBS depth profiling. *Mater. Adv.* **2022**, *3*, 7846–7853. [CrossRef]
7. Weller, M.T.; Weber, O.J.; Frost, J.M.; Walsh, A. Cubic perovskite structure of black formamidinium lead iodide, α-$[HC(NH_2)_2]PbI_3$, at 298 K. *J. Phys. Chem. Lett.* **2015**, *6*, 3209–3212. [CrossRef]
8. Zuo, L.; Li, Z.; Chen, H. Ion migration and accumulation in halide perovskite solar cells. *Chin. J. Chem.* **2023**, *41*, 861–876. [CrossRef]
9. Thiesbrummel, J.; Milić, J.V.; Deibel, C.; Garnett, E.C.; Tao, S.; Kirchartz, T.; Guerrero, A.; Cameron, P.; Tress, W.; Islam, M.S.; et al. Ion migration in perovskite solar cells. *Nat. Rev. Chem.* **2026**, *10*, 179–195. [CrossRef] [PubMed]
10. Mokgolo, P.J.; Gumede, T.P.; Ocaya, R.O.; Malevu, T.D. Enhancing perovskite solar cells with rare-earth metal doped zinc oxide: A review of electron mobility, stability, and photocarrier recombination. *Int. J. Energy Res.* **2025**, *2025*, 4240199. [CrossRef]
11. Terribili, L.; Rateau, R.; Szucs, A.M.; Maddin, M.; Rodriguez-Blanco, J.D. Impact of rare earth elements on $CaCO_3$ crystallization: Insights into kinetics, mechanisms, and crystal morphology. *Cryst. Growth Des.* **2024**, *24*, 632–645. [CrossRef] [PubMed]
12. Okumura, R.; Oku, T.; Suzuki, A.; Okita, M.; Fukunishi, S.; Tachikawa, T.; Hasegawa, T. Electronic structures and photovoltaic properties of copper-, sodium- and ethylammonium-added $CH_3NH_3PbI_3$ perovskite compound. *Eng. Proc.* **2022**, *31*, 29. [CrossRef]
13. Khorshidi, E.; Rezaei, B.; Blätte, D.; Buyruk, A.; Reus, M.A.; Hanisch, J.; Böller, B.; Müller-Buschbaum, P.; Ameri, T. Hydrophobic graphene quantum dots for defect passivation and enhanced moisture stability of $CH_3NH_3PbI_3$ perovskite solar cells. *Sol. RRL* **2022**, *6*, 2200023. [CrossRef]
14. Wang, H.; Zou, W.; Ouyang, Y.; Liu, X.; Li, H.; Luo, H.; Zhao, X. Potassium salt coordination induced ion migration inhibition and defect passivation for high-efficiency perovskite solar cells. *J. Phys. Chem. Lett.* **2022**, *13*, 8573–8579. [CrossRef] [PubMed]
15. Tanaka, R.; Suzuki, A.; Oku, T.; Tachikawa, T.; Fukunishi, S. Formation of orthorhombic $CH_3NH_3PbI_3$ perovskite co-doped with ytterbium and gadolinium. *Chem. Phys. Lett.* **2024**, *856*, 141679. [CrossRef]
16. Chang, Q.; Wang, F.; Xu, W.; Wang, A.; Liu, Y.; Wang, J.; Yun, Y.; Gao, S.; Xiao, K.; Zhang, L.; et al. Ferrocene-induced perpetual recovery on all elemental defects in perovskite solar cells. *Angew. Chem. Int. Ed.* **2021**, *60*, 25567–25574. Correction in *Angew. Chem. Int. Ed.* **2022**, *61*, e202204273. https://doi.org/10.1002/anie.202204273. [CrossRef] [PubMed]

17. Liao, M.; Tang, S.; Liu, J.; Sun, W.; Wu, J.; Xie, Y.; Lu, C.-Z. Rare earth polyoxometalates for enhanced performance of carbon-based all-inorganic $CsPbBr_3$ perovskite solar cells. *Surf. Interfaces* **2025**, *72*, 107326. [CrossRef]
18. Patil, J.V.; Mali, S.S.; Hong, C.K. Holmium rare earth metal ion incorporated and ambient-air processed all-inorganic γ-$CsPbI_{2.5}Br_{0.5}$ perovskite solar cells yielding high efficiency and stable performance. *J. Mater. Chem. A* **2023**, *11*, 21312–21321. [CrossRef]
19. Zhou, M.; Wang, T.; Li, F.; Li, K.; Zhao, X.; Cai, Z.; Lu, X.; Sun, S.; Li, Z.; Li, D.; et al. Thermally driven lanthanide dual-site doping enables high-performance perovskite solar cells via halide migration suppression. *Carbon Neutraliz.* **2026**, *5*, e70087. [CrossRef]
20. Zeng, Z.; Xu, Y.; Zhang, Z.; Gao, Z.; Luo, M.; Yin, Z.; Zhang, C.; Xu, J.; Huang, B.; Luo, F.; et al. Rare-earth-containing perovskite nanomaterials: Design, synthesis, properties and applications. *Chem. Soc. Rev.* **2020**, *49*, 1109–1143. [CrossRef] [PubMed]
21. Chen, Y.; Liu, S.; Zhou, N.; Li, N.; Zhou, H.; Sun, L.-D.; Yan, C.-H. An overview of rare earth coupled lead halide perovskite and its application in photovoltaics and light emitting devices. *Prog. Mater. Sci.* **2021**, *120*, 100737. [CrossRef]
22. Huang, C.; Li, P.; Li, X.; Gu, J.; Fu, N.; Zhang, W. Applications of rare-earth-based up-conversion and down-conversion in perovskite solar cells: A review. *Sol. RRL* **2023**, *7*, 2300518. [CrossRef]
23. Yang, Y.; Wu, J.; Wang, X.; Guo, Q.; Liu, X.; Sun, W.; Wei, Y.; Huang, Y.; Lan, Z.; Huang, M.; et al. Suppressing vacancy defects and grain boundaries via Ostwald ripening for high-performance and stable perovskite solar cells. *Adv. Mater.* **2020**, *32*, 1904347. [CrossRef] [PubMed]
24. Luo, Q.; Yu, J.; Deng, X.; Cao, M.; Ma, S.; Hua, Q.; Xue, D.; An, F. Preparation of $NaYF_4$:Tm, Yb, and Gd luminescent nanorods/SiO_2 nanospheres composite thin film and its application in perovskite solar cells. *Materials* **2023**, *16*, 6917. [CrossRef] [PubMed]
25. Chai, W.; Zhu, W.; Xi, H.; Chen, D.; Dong, H.; Zhou, L.; You, H.; Zhang, J.; Zhang, C.; Zhu, C.; et al. Buried interface regulation with $TbCl_3$ for highly efficient all-inorganic perovskite/silicon tandem solar cells. *Nano-Micro Lett.* **2025**, *17*, 244. [CrossRef] [PubMed]
26. Li, Y.; Xu, Y.; Du, K.; Zhou, C.; Ding, J.; Li, L.; Yuan, N. Cerium rare-earth ions reinforced built-in electric field to enable efficient carrier extraction for highly efficient and stable perovskite solar cells. *J. Alloys Compd.* **2024**, *1005*, 176066. [CrossRef]
27. Tanaka, R.; Suzuki, A.; Oku, T.; Tachikawa, T.; Fukunishi, S. Effect of co-doping of ytterbium and neodymium to $CH_3NH_3PbI_3$ perovskite solar cells. *Mater. Chem. Phys.* **2026**, *350*, 131889. [CrossRef]
28. Yamamoto, K.; Suzuki, A.; Okumura, R.; Enomoto, A.; Ono, I.; Oku, T.; Fukunishi, S.; Tachikawa, T.; Hasegawa, T. Effects of neodymium or ytterbium addition to $CH_3NH_3PbI_3$ perovskite solar cells inserted with decaphenylcyclopentasilane. *Results Surf. Interfaces* **2024**, *15*, 100224. [CrossRef]
29. Nakamura, R.; Suzuki, A.; Shimada, H.; Nasu, T.; Oku, T.; Tachikawa, T.; Fukunishi, S. Fabrication and characterization of lanthanide-doped perovskite solar cells. *Appl. Surf. Sci.* **2026**, *728*, 166156. [CrossRef]
30. Yu, Z.; Chan, W.K.; Zhou, D.; Li, X.; Lu, Y.; Jiang, Z.; Xue, B.; Zhu, H.; Dowland, S.; Ye, J.; et al. Overcoming lattice mismatch for core-shell $NaGdF_4$@$CsPbBr_3$ heterostructures. *Nat. Commun.* **2025**, *16*, 3891. [CrossRef] [PubMed]
31. Zhang, S.-Y.; Guo, X.; Xu, Y.-M.; Jiao, Y.; Lin, Z.-H.; Zhang, J.-C.; Ouyang, J.-Y.; Guo, L.-X.; Hao, Y.; Chang, J.-J. Optimizing ETL/$CsPbBr_3$ buried interface contact for enhanced efficiency and stability of inorganic perovskite solar cells. *Rare Met.* **2025**, *44*, 3069–3079. [CrossRef]
32. Nakamura, R.; Suzuki, A.; Oku, T.; Tachikawa, T.; Fukunishi, S. Effects of lanthanoid codoping on hysteresis suppression, long-term stability, and fill factor improvement in perovskite solar cells. *Phys. Status Solidi A* **2026**, *223*, e70466. [CrossRef]
33. Okumura, R.; Oku, T.; Suzuki, A. Electronic structures of ABX_3 perovskite crystals with a monovalent copper ion as the A-site cation. *Chem. Phys. Impact* **2024**, *8*, 100534. [CrossRef]